Research Article | Vol. 32, No. 2 / 15 Jan 2024 / *Optics Express* 1609

Optics EXPRESS

Spherical wave illumination scanning digital holographic profilometry

Kai Wen,[1,2,†] Moncy Sajeev Idicula,[1,†] Michał Józwik,[1] Hyon-Gon Choo,[3] Peng Gao,[2] and Tomasz Kozacki[1,*]

[1] *Faculty of Mechatronics, Institute of Micromechanics and Photonics, Warsaw University of Technology, 02-525, Warsaw, Poland*
[2] *School of Physics, Xidian University, Xi'an 710071, China*
[3] *Electronics and Telecommunications Research Institute, Daejeon 34129, Republic of Korea*
[†] These authors contributed equally to this work.
[*] *tomasz.kozacki@pw.edu.pl*

Abstract: In this work, we proposed what we believe to be a novel scanning solution for the assessment of high-NA samples, referred to as spherical-wave illumination scanning digital holographic profilometry (SWS-DHP). This approach introduces a 2F optimization methodology, based on the measurement of the focal length of the object to determine the spherical component of the scanning. Furthermore, re-optimization of 2F, whether it needs to be operated depends on the measured object's NA to inspect more information. Meanwhile, utilizing phase space analysis shows SWS superiority in information transfer for high-NA samples compared to plane-wave illumination scanning. In addition, this method introduces a shape reconstruction algorithm with volumetric aberration compensation based on the propagation of the aberrated object and illumination waves to obtain high-quality measurements. Finally, the imaging merits of SWS-DHP were proved through simulations and were experimentally verified for the object of NA up to 0.87.

1. Introduction

Optical imaging is a commonly used morphometric technique that images and measures the surface of the test sample through the use of an optical microscope, which plays an essential role in industries, materials science, biomedicine, and other fields. Digital holographic microscopy (DHM) is a non-invasive, quick interferometric method that stands out due to phase measurement accuracy [1–3], which has been further improved recently thanks to deep learning techniques [4–6] and is widely used in various fields such as surface profile measurement [7–9]. However, it is worth noting that the use of plane-wave illumination in DHM is not optimal from the point of view of the achieved resolution of the reconstructed image, i.e., the entire sample information cannot be obtained under the limited numerical aperture (NA) of the setup. The combination of structured and oblique illumination with DHM solves this drawback, increasing the resolution of the measurement and consequently enabling the reconstruction of fine details of the sample [1,10–12]. What is more, limited resolution is also important for optical profilometry, and researchers resort to illumination optimization for obtaining more information about the sample [13,14].

Meanwhile, traditional DHM utilizes digital processing methods of one or multi-phase-shifting holograms to simultaneously provide reconstructed amplitude and phase images. However, a limitation of the phase information obtained through DHM is that it is only defined with a 2π range. This means an additional step called phase unwrapping is needed to obtain continuous phase distribution [2,15]. Furthermore, the traditional DHM method uses plane-wave illumination and

#507233 https://doi.org/10.1364/OE.507233
Journal © 2024 Received 28 Sep 2023; revised 10 Nov 2023; accepted 10 Nov 2023; published 3 Jan 2024

does not facilitate the measurement of objects with discontinuities higher than λ/4 (in reflection mode) or high-NA shape measurements. The limitation associated with discontinuities is known as the 2π ambiguity problem, and this problem can only be solved using multiple illumination angles or wavelengths [7]. For solving high-NA limitation, methods using spherical-wave illumination were proposed, however, the solutions are based on phase unwrapping and are therefore limited to samples with continuous phase distribution due to the 2π ambiguity problem [14,16,17]. Moreover, holographic techniques can achieve precise measurements of high-NA samples, but only if the in-focus plane of an imaging system is determined with high accuracy. However, realizing this requirement results in a significantly complicated optical setup [18].

Many techniques have already been proposed to solve the 2π ambiguity problem. One of the methods is called multi-wavelength interferometry (MWI). It uses a dye laser tuned at three different wavelengths [19], a tunable diode laser at different wavelengths [20,21], or two/three separate lasers [22,23] to enlarge the unambiguous measurement range (UMR) with a synthetic wavelength much larger than the original wavelength [24]. Notably, while MWI can obtain large discontinuity depth measurements, the limited tuning range, wavelength control accuracy, and instability make the setup of MWI becomes more complex. At the same time, MWI may get inaccuracy results because of the chromatic aberration due to different wavelengths if the reflection of the test sample is wavelength-dependent [15].

The 2π ambiguity problem can also be solved as well by illuminating the object with different illumination angles, which is referred to as plane-wave scanning. One of the well-known techniques using this concept is optical contouring, where two holograms are captured at different illumination angles [25]. Although this method can extract phase from each corresponding contour line of holograms, which contains the height distribution, its axial resolution is limited due to the use of two illumination angles, which must be close to each other ($\delta_\theta < 0.1°$) [26]. At the same time, multi-angle interferometry (MAI) can measure the object over a larger unambiguous measurement range (UMR) than optical contouring, because it uses more than two different illumination angles holograms [15]. However, its axial resolution is still limited by the allowed angular illumination span ($\delta_\theta = 0.5°$-$1°$). Unlike those mentioned above, a new approach combining MAI and multi-beam illumination of coherence holography [27] was proposed to solve the limitation of the axial resolution of surface reconstruction and get a large UMR [7–9]. It is worth noting that all reported MAI solutions use plane-wave illumination to capture information about the measured object. This illumination method is not optimal in terms of capturing information for limited NA of imaging optics, making MAI ineffective for measuring high-NA objects.

On the contrary, this work presents a scanning solution where the measured object is illuminated by waves that combine spherical and plane waves, referred to as spherical-wave illumination scanning digital holographic profilometry (SWS-DHP), and enables the measurement of high-NA samples. To define the sphericity parameters of SWS, we introduce a 2F optimization method based on measuring the focal length of an object to determine the spherical component of the scanning. This method can measure successful the objects with NA (0.47 and 0.52), while re-optimization on 2F is necessary for an object with a NA surpassing 0.87. The optimization used in this case was based on the inspection of information transfer from the high-NA object area. The introduced SWS illumination strategy is theoretically investigated using phase space (PS) analysis, demonstrating its superiority in information transfer for high-NA samples compared to plane wave-based MAI. At the same time, conventional holographic aberration compensation based on aberration subtraction proved ineffective in large aperture field measurements. It is worth mentioning that this method has been used in all our previous works [7,8]. Therefore, in this work, we introduce a shape reconstruction algorithm with volumetric aberration compensation based on the propagation of aberrated objects and illumination waves, which enables measurements of high-NA samples. The characteristics of the introduced SWS-DHP and its functional advantage are demonstrated by using numerical and optical experiments.

2. Experimental setup and methods

2.1. Digital holographic profilometry with spherical-wave illumination scanning

A schematic diagram of digital holographic profilometry system with spherical-wave illumination scanning (SWS-DHP) is shown in Fig. 1. This optical setup is based on the Twyman-Green interferometer, and the coherent illumination source is a 532-nm Nd-YAG diode laser. After passing through a neutral density filter, the intensity of the illumination beam is attenuated and becomes elliptically polarized by a quarter-wavelength plate (QP, AQWP10M-600, Thorlabs). Then, it is reflected by mirror M_1 and divided by a polarizing beam splitter (PBS). One of the illumination beams, which is used for the object wave, has a linear polarization aligned by the half-wavelength plate (HP, AHWP10M-600, Thorlabs) to achieve maximum modulation of the spatial light modulator (SLM). In addition, the second beam, called the reference wave, is reflected by mirror M_2 and gets through the polarizer P and HP to receive the same polarization as the object wave. Differently, the coherence of the object wave is improved by using a spatial filter (SF), then the object wave is collimated by L_1 and illuminating SLM (HOLOEYE, GAEA-2, resolution 4160×2464, pixel size 3.74 µm). For realizing plane-wave scanning SLM is sequentially loaded with plane-wave patterns (Fig. 1(a_1)), while for spherical-wave scanning with a combination of plane-wave and spherical-wave patterns, respectively. Figure 1(a_1) and Fig. 1(a_2) show a series of components example fringe patterns for spherical-wave scanning. Notably, the sphericity used to generate the image pattern depends on the overall system magnification and the object under test. The required sphericity will help us to acquire as much information as possible for the high-NA samples. Furthermore, the diffracted beams along different directions are generated and reflected by an optical wedge W_1. And the illumination beam is relayed to the sample plane by two afocal systems, i.e., lenses L_2 and L_3 ($f_2 = f_3 = 125$ mm, AC254-125-A-ML, Thorlabs) and lens L_5 ($f_5 = 200$ mm, AC254-200-A-ML, Thorlabs), and microscope objective (MO). A frequency filtering mask is placed between the focal plane of L_2 and lens L_3, which only allows the $+1^{st}$ order to pass through while blocking all other diffraction orders. It is essential to mention that we need to move the size-adjustable filter mask along the optical axis to the focus point of the scanning wave, as shown in Fig. 1(b). Its location depends on the NA of the measured object and applied sphericity of scanning. Moreover, the mask has the same dimension of 1.5 mm $\times$ 8 mm when realizing plane-wave and spherical-wave illumination. The filtered $+1^{st}$ diffraction order is reflected by mirror (M_4) and then illuminates the sample through the $4f$ system (consisting of L_5 and MO). The beam reflected by the object surface containing the sample information passes through an optical wedge W_2, interfering with the collimated reference wave through SF and L_4 at the CMOS camera (Basler, piA2400-12gm/gc, resolution 2464×2056, pixel size 3.45 µm) plane.

At the same time, we select the equally angle-spaced strategy [7,8] to ensure the good metrological properties of the longitudinal scanning function (LSF). In addition, this strategy enables maintaining an extensive unambiguous measurement range and high resolution of reconstruction. The schematic of the SWS illumination method along the y direction is shown in Fig. 1(c). The angular range and step are [-17°, 17°] and 1° when using a 20× Mitutoyo microscope objective with 0.42 NA in the experiment, which means we need to capture 35 holograms. Besides this, for higher resolution measurements we also use a 50× Mitutoyo microscope objective with 0.75 NA with scanning along the y direction from -30° to 30°. A total number of 61 holograms were captured to ensure the accuracy of the shape reconstruction. The spherical component of SWS that needs to be introduced onto the SLM to generate spherical illumination wave is limited to 55.4 µm as the minimum focal. Notably, this sphericity parameter depends on the $4f$ system (consisting of L_2 and L_3) and the pixel size of SLM used.

Optics EXPRESS

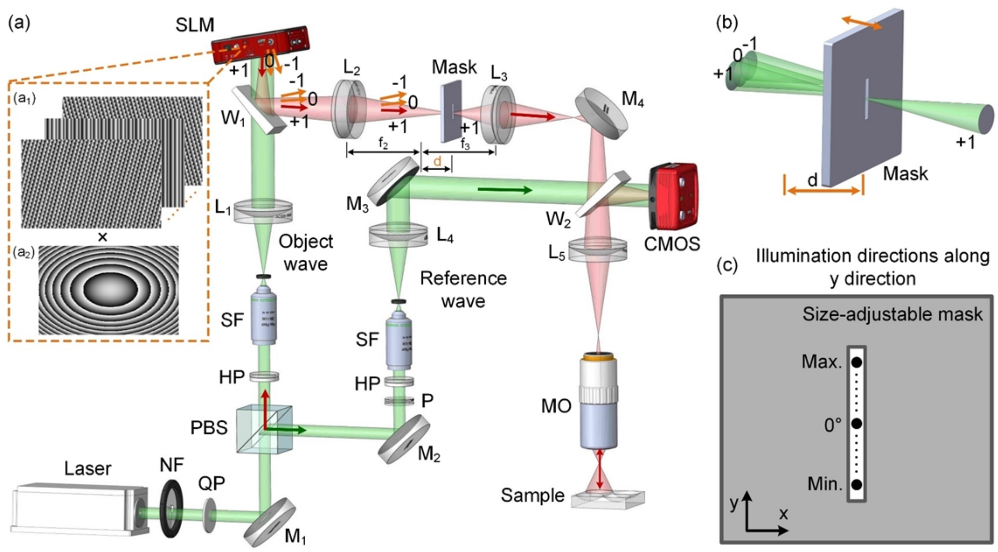

Fig. 1. The schematic diagram of the SWS-DHP system. (a) The experimental setup. The inset shows the combination of illumination patterns to realize spherical-wave illumination scanning: (a_1) plane-wave and (a_2) spherical-wave components. (b) The filter mask is placed between the lens L_2 and L_3. (c) Positions of illumination beam during the scanning along *y* direction used in the experiment. Max. and Min. are the maximum and minimum illumination angles, respectively. HP, half-wavelength plate; L_1-L_5, achromatic lens; M_1-M_4, mirrors; MO, microscope objective; NF, neutral density filter; W_1-W_2, optical wedge; P, polarizer; PBS, polarizing beam splitter; QP, quarter-wavelength plate; SF, spatial filter; SLM, spatial light modulator.

2.2. Characteristics of spherical-wave illumination scanning

Figure 2 shows the advantage of spherical-wave scanning (SWS) over plane-wave one in terms of transferred information for the measured sample with high-NA. When plane-wave scanning is used to illuminate a sample with a high-NA, a large part of the reflected beam cannot pass through the MO, resulting in a lack of object information encoded in the hologram, as shown by the red dashed line in Fig. 2(b). Too small NA of MO causes this problem. In this paper, to solve this problem, we introduce an illumination optimization to the shape of the measured sample so that the illumination falls approximately normally on the entire surface. In this way, the beam reflected from the object has a reduced NA, and full information about the measured sample can be encoded in the hologram, as illustrated in Fig. 2(c). Here, we just simply use the results of 0° angle to analyze the advantage of SWS. However, this does not prove that the proposed scanning solution, which is optimized for angle 0°, is also optimal over the entire scanning range. Hence, we better illustrate this problem in the following part through the phase space (PS) analysis.

The above discussion presents the NA optimization concept for a scanning angle of 0°, while the SWS has two components: a spherical-wave and a plane-wave. Its distribution can be described as:

$$u_{sws(\theta)}(x,y) = exp\{ik\sqrt{x^2+y^2+{z_s}^2}\}exp\{2\pi i f_{ys(\theta)}y\}, \tag{1}$$

where $f_{ys(\theta)} = \sin(\theta_{ys(\theta)})/\lambda$ is a frequency related to the scan angle and z_s is a focus distance of the spherical component. The plane-wave component depends on the NA of MO, as discussed in Sec. 2.1 is defined by the scan angle $\theta_{ys(\theta)}$. The spherical component depends on NA of the object measured, and it is defined by z_s. First, for finding z_s, hologram with the object for 0° plane wave illumination is captured. Then, the hologram is reconstructed and processed using the angular

Optics EXPRESS

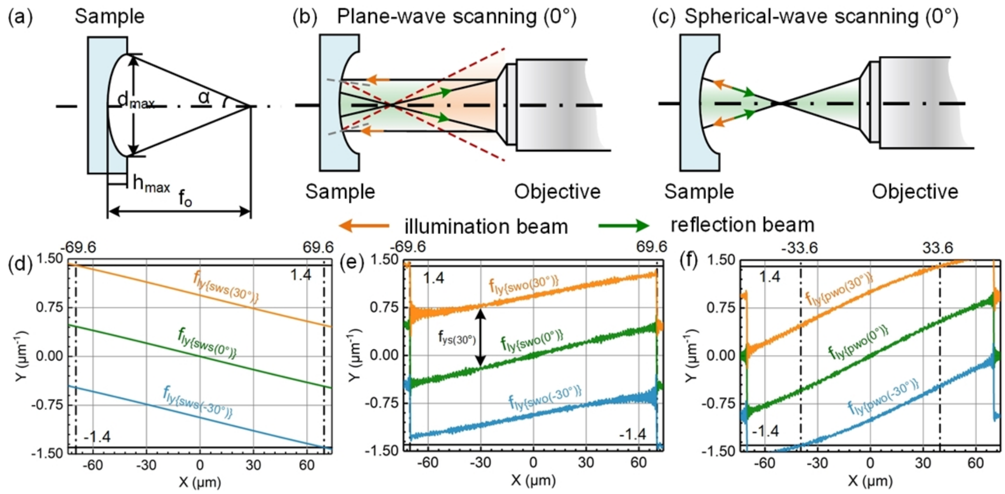

Fig. 2. The schematic phase space analysis of the plane and spherical wave illumination scanning. (a) Simulated sample. (b) and (c) are the schematic of the plane and spherical wave illumination scanning of 0° angle, respectively. (d) The frequency distribution of spherical-wave illumination scanning without the object. (e-f) Phase Space Analysis of the two illumination scanning methods set applied for the spherical object.

spectrum propagation method to measure the focal length f_o of the object, and the final $z_s = 2f_o$. The focal length of the micro object is the distance between the object vortex and the point of beam focus (Fig. 2(a)). This method of finding the spherical components of SWS is referred to as 2F optimization method. To approximate the NA of the objects, we can use the relation $NA_{approx} = \sin(\alpha)$, and $\alpha = \arctan(d_{max}/2(f_o - h_{max})$, where d_{max} is the diameter of the object and h_{max} is the height of the object [28], as shown in Fig. 2(a). Notably, this approximate relation uses the beam from the surface of the object to calculate and is only available for plane-wave illumination under the reflected mode. For this work, we use three objects with different NA and the parameters as shown in Table 1.

Table 1. The parameters of the samples.

Name	Outer Shape	*Magnification*	d_{max} [μm]	f_o [μm]	h_{max} [μm]	NA
Sample 1	Square	50×	211	187	13.3	0.52
Sample 2	Square	20×	268.5	270	15.0	0.47
Sample 3	Hexagon	50×	148	68	20.6	0.84

A high-NA object has different gradients in different areas, and the object beam encodes this gradient in the different frequencies regions. To test illumination performance of the SWS, we analyze the local NA of the object beam. For this purpose, PS analysis is used, which provides access to local spatial frequency information [29]. To calculate the PS distribution of the wave u, the local spatial frequencies concept is used [30], which for x direction is determined as:

$$f_{lx}(x, y) = \frac{1}{2\pi} \frac{\delta ARG\{u(x, y)\}}{\delta x}. \quad (2)$$

In this way, the local spatial frequency (f_{lx}, f_{ly}) is determined for the corresponding spatial position (x, y), and ARG means the phase of u. In this section, calculations are made for the model beam and for the simulation results. The PS is applied for the object presented in Fig. 2(a), which has $NA = 0.5$ ($d_{max} = 140\,\mu m$, $h_{max} = 8.8\,\mu m$, $f_0 = 138\,\mu m$). The object under study has a

Optics EXPRESS

high-NA, and the SWS uses large angles, so a paraxial approximation cannot be used. Therefore, the PS analysis shown is based on a wave simulation in which the scanning wave illuminates the object under study. Simulation of the reflection of an illuminating beam by an object is performed using the wave scattering method (WSM) [31]. WSM is calculating scattered wave components using the integral equation of scattering potential [32]. A frequency implementation of WSM was proposed in Ref. [33], in which it was shown that the approach can accurately simulate refraction or reflection from a micro-surface. However, the method loses its numerical effectiveness if non-plane-wave illumination is used. In the implementation of Ref. [31], the solution is based on computation layer by layer, resulting in high computational efficiency also for simulating arbitrary illumination waves. Moreover, this study assumes that the optical system accepts a frequency range between $-1.4\ \mu m^{-1}$ and $1.4\ \mu m^{-1}$ (using 0.75 NA and λ=532 nm). Solid lines along the horizontal direction show this frequency range in Fig. 2(d-f). At the same time, using the black dash-dotted vertical lines shows the maximum extent of the object that can be measured with full performance. For this object, the found spherical parameter of the scanning $z_s = 276\ \mu m$. Phase space distribution (PSD) of the employed SWS is presented in Fig. 2(d) for the y direction for the 0° and limiting angles. It can be calculated using the local spatial frequency concept [30], which, when applied to Eq. (1) is given as:

$$f_{ly\{sws(\theta)\}} = \frac{1}{2\pi}\frac{\delta ARG\{u_{sws(\theta)}\}}{\delta y} = \frac{1}{\lambda}\frac{y}{\sqrt{x^2+y^2+{z_s}^2}} + f_{ys(\theta)}. \tag{3}$$

This shows that the local spatial frequency of the scanning has two independent elements, spherical and plane wave, where the plane-wave component is shifting the spherical-wave component, thus, the presented PSD for 0° for y also represents the local spatial frequency for x. Notably, the spherical wave component is approximately line of tangential $\lambda^{-1}{z_s}^{-1}$. In Fig. 2(d-f), three different distributions are presented for −30°, 0°, and 30°. 30° corresponds to the spatial frequency $f_{ys(30^{\circ})} = 0.94\ \mu m^{-1}$. Figure 2(e) presents PSD when applying the SWS to the object, where the object wave simulated using the wave scattering method is denoted as $u_{swo(\theta)}$. Its PSD is calculated directly by using the definition given by Eq. (2). The results obtained, denoted as $f_{ly\{swo(\theta)\}}$, are presented in Fig. 2(e). Comparing Fig. 2(d) and 2(e), one can see the similarity between the PSD of illumination and object waves obtained for SWS. This resemblance is obtained because the optimal illumination condition was chosen, for which we can write the space-frequency condition as

$$f_{ly\{sws(\theta)\}}(x,y) + f_{ly\{swo(\theta)\}}(x,y) \approx 0. \tag{4}$$

This condition means that the absolute values of the local spatial frequencies of the illumination and object wave are equal. As a result, this optimal illumination minimizes the bandwidth of the illumination and object wave, and all the high-NA information can be accepted by the optical system. However, as shown in Fig. 2(f), the optimal illumination condition for the plane-wave scanning is not met because the local spatial frequency of the spherical wave component for plane-wave scanning is approximately twice larger than for SWS. As a result, local spatial frequencies are increased for some areas. Thus, the bandwidth of the object wave exceeds the NA of the optical system, causing a loss of information about the object's high-NA areas. This point is proved by the results of Fig. 2(d-f), in which for the y-direction, the measurement area of the plane-wave illumination is −33.6 μm to 33.6 μm, but the measurement are of the SWS is −69.6 μm to 69.6 μm.

In addition, it is worth noting that the use of appropriate sphericity (z_s) for spherical-wave illumination scanning is crucial, as sphericity affects the acquisition of sample information. Different samples require the selection of the appropriate sphericity to ensure the acquisition of as much information as possible. The 2F illumination optimization method is able to find the spherical parameters for the presented objects with high-NA. Here, it can be applied to measure sample 1 of NA = 0.52 and sample 2 of NA = 0.47. However, we find that for very high-NA objects, the sphericity of scanning (z_s) may need to be reoptimized according to the gradient and complexity of the sample when starting the experiment.

Here, an asymmetrical and aspherical high-NA object (sample 3 with NA = 0.84) was chosen to prove the capability of SWS-DHP with a need for re-optimization of scanning sphericity. Without this sphericity re-optimization SWS-DHP is providing measurements in a limited area because of the complex shape of the object. Therefore, to illustrate the need for additional optimization, we compared the holograms (with and without sample 3 and their corresponding spectra for z_s 136 µm and 200 µm. Notably, 136 µm is calculated by using the 2F optimization method, and 200 µm is the value after SWS re-optimization for this specific sample 3. The re-optimization was realized by viewing the spatial distribution of the hologram of the illumination and the object for different scan angles. The Fig. 3-left part shows the results for illumination angles of 0°, 10°, and 20° and the sphericity of 136 µm, and the Fig. 3-right part is for 200 µm. We can find that using the sphericity of $z_s = 200$ µm enables to encode more information about the same sample in the hologram, whatever illumination angle is used, after comparing Fig. 3(a, e, i) and Fig. 3(c, g, k). Meanwhile, by comparing the spectrums for different angles, 200 µm (Fig. 3(d, h, l)) contains more information about the sample than 136 µm (Fig. 3(b, f, j)). Note that this additionally optimized SWS guaranteed a successful measurement for sample 3; without it, shape reconstruction was impossible.

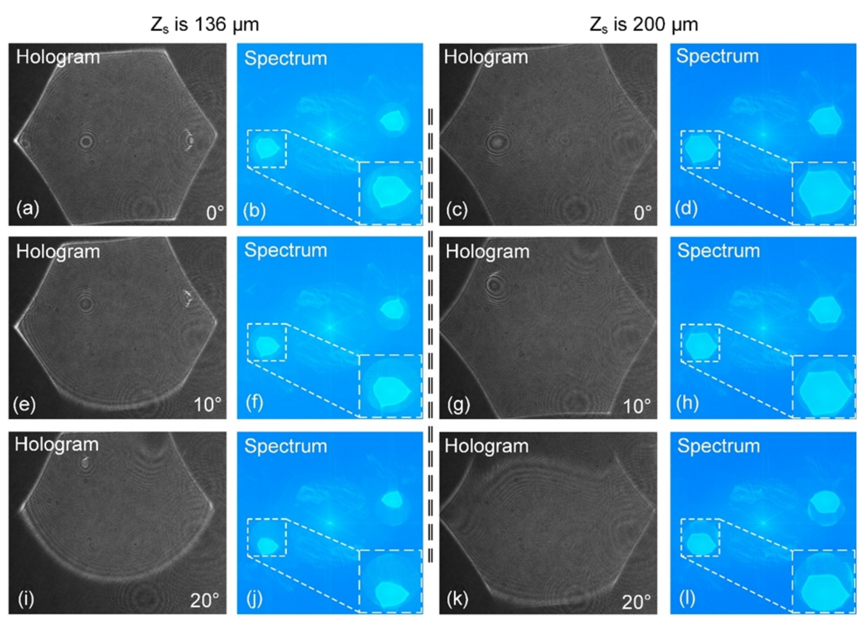

Fig. 3. Results of spherical-wave illumination scanning method using $z_s = 136$ µm and $z_s = 200$ µm sphericity. (a), (e), and (i) are the holograms of different illumination angles for imaging the hexagon using 136 µm sphericity. (c), (g), and (k) are the holograms of different illumination angles for imaging the hexagon using 200 µm sphericity. (b), (d), (f), (h), (j), and (l) are the corresponding frequency spectrum of (a), (c), (e), (g), (i), and (k).

As shown in Fig. 4, we compare the hologram and Fourier spectrum for plane-wave and SWS illumination for 0° and -15° angles. Comparing these results, when the object is illuminated with a plane-wave, as shown in Figs. 4(f) and 4(n), the object beam occupies the entire frequency of the limited NA of the system. However, as shown in Figs. 4(e) and 4(m), it contains less spatial information about the object. The high-NA information of the object is lost. Differently,

Optics EXPRESS

it acquires more spatial information when SWS is employed for the same object, as shown in Fig. 4(g) and 4(o), which shows all the information now fits inside the limited NA of the setup from Fig. 4(h) and 4(p). The PS analysis employed above also proves that plane-wave illumination is not the optimal illumination method, it shows that one has to look at space and frequency domain representation of the beam. At the same time, the SWS method is able to fit all object frequencies in the NA of the system. For shape reconstruction from the captured data, it is necessary to obtain all the information about the object, therefore, it is clear that for plane-wave illumination, some part of the data will always be missing, whereas more information will be passed irrespective of illumination angle using the SWS method. As mentioned in Section 2.3, we need to consider the effect of illumination wave for shape reconstruction, hence, we capture the holograms with a reference mirror (for the case without a sample), as shown in Fig. 4(a), 4(c), 4(i), and 4(k). At the same time, we compare the corresponding spectrum under 0° and −15° illumination angles of all holograms. From the spectrum, even with or without the sample, the big boundary of spatial frequency will be blocked by the limited NA of micro-objective. This point has the same effect on both illumination scanning methods, spherical-wave illumination scanning still contains more spatial information of the same conditions. Furthermore, rectangle area of the spectrum (shown in Fig. 4(d) and 4(l)) by spherical-wave illumination scanning is caused by the pixel of SLM.

2.3. Reconstruction algorithm with volumetric aberration compensation

Our previous work introduced the shape reconstruction algorithm based on plane-wave illumination [7–9]. Since the illumination method of this work is different, i.e., SWS, the reconstruction algorithm based on plane-wave cannot be used. Moreover, the previous algorithm is based on the implementation of the model of plane-wave. This illumination-model approach requires subtraction of the aberration at the hologram plane. During the development of this work, we investigated this model-based approach, where propagation of the model of the spherical-wave was considered. The parameters of the model beam were found by its measurement with least-square fitting. However, it turned out that this approach based on the illumination model was not effective, we could not obtain correct measurements. This is because the conventional aberration compensation method, which is based on subtraction, is too inaccurate for high-aperture fields. Therefore, the approach used is based on the propagation of the object and the illumination waves, where both waves are measured. In this way, aberrations are automatically corrected within entire 3D volume of the reconstruction. Consequently, the proposed shape reconstruction algorithm allows the use of arbitrary illumination beams and provides accurate aberration compensation for all depths of the reconstruction. In Fig. 5, the flowchart illustrates the computational process required for the sample shape reconstruction using SWS, which contains pre-processing and shape reconstruction based on LSF calculation parts.

The pre-processing part can be described as steps:

1) The holograms with sample (I_{om}) and without sample (I_{im}) captured using the multi-angle illumination are digitally retrieved, and then the corresponding complex amplitudes $U_{\mathrm{om}}(x, y, 0)$ and $U_{\mathrm{im}}(x, y, 0)$ are obtained sequentially.

2) Considering the influence of slight defocus, as shown in Fig. 5(i), $U_{\mathrm{om}}(x, y, 0)$ and $U_{\mathrm{im}}(x, y, 0)$ are propagated using the angular spectrum propagation (ASP) [34] method to the distance z_{o} (with samples) and z_{i} (without samples), and it can be explicitly described as:

$$U(x, y, z) = \mathrm{IFT}\left\{\mathrm{FT}[U(x, y, 0)] \exp\left[izk\sqrt{1 - (\lambda k_{xm})^2 - (\lambda k_{ym})^2}\right]\right\}, \tag{5}$$

where k_{xm} and k_{ym} are the spatial coordinates of multi-angle. FT and IFT are the Fourier transform and inverse Fourier transform, respectively. z_{o} and z_{i} are the defocusing distances of the sample and reference mirror (for the case without a sample).

Optics EXPRESS

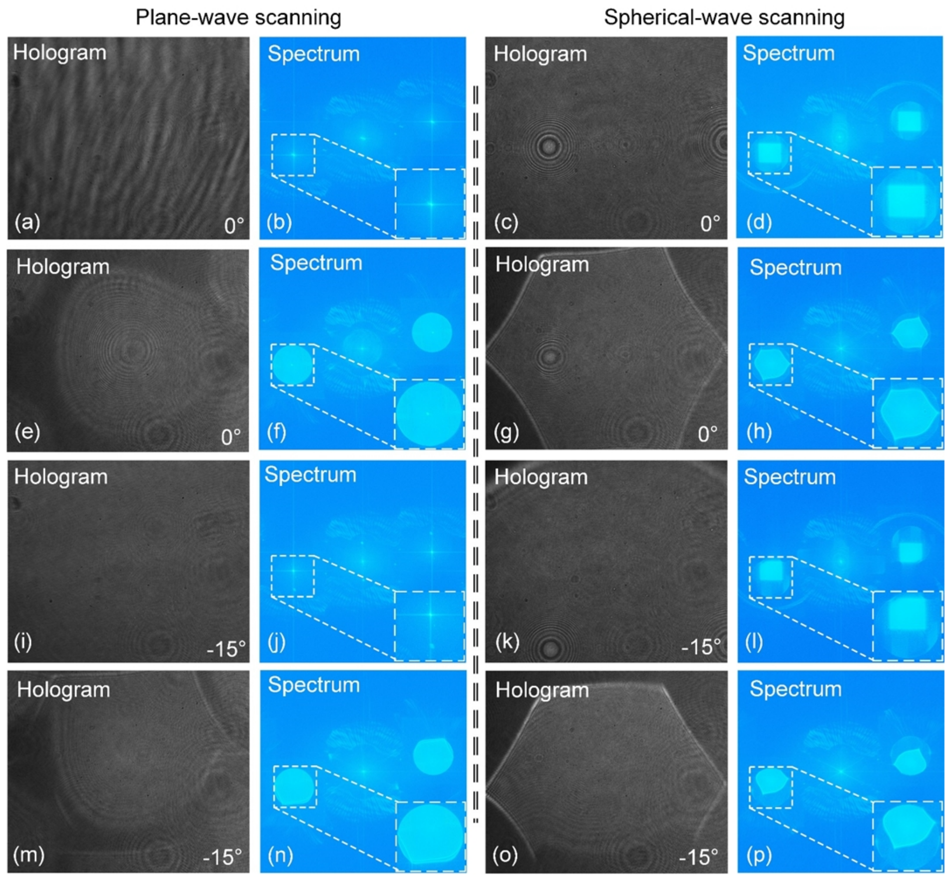

Fig. 4. Comparison of results between plane-wave scanning and spherical-wave scanning illumination methods. (a), (c), (i), and (k) are the holograms of different illumination angles in the absence of samples under two methods. (e), (g), (m), and (o) are the holograms of different illumination angles with samples under two methods. (b), (f), (j), and (n) are the corresponding frequency spectrum of (a), (e), (i), and (m). (d), (h), (l), and (p) are the corresponding frequency spectrum of (c), (g), (k), and (o).

The shape reconstruction part based on LSF calculation can be described as follows:

3) As shown in Fig. 5(ii), after obtaining the complex amplitude of $U_{\mathrm{om}}(x, y, z_{\mathrm{o}})$ and $U_{\mathrm{im}}(x, y, z_{\mathrm{i}})$, an aberration compensation operation is performed for every illumination angle of the same propagation step z.

4) LSF (x, y, z) is calculated as the summation of all the complex fields obtained after step 3:

$$LSF(x, y, z) = \left| \sum_{m} U_{\mathrm{om}}(x, y, z + z_o) U_{im}(x, y, z + z_i)^* \right|. \tag{6}$$

5) Propagation step (z) is increased $z = z + \delta z$, and steps 3 to 4 are repeated, see Fig. 5(iii).

6) The values of z, having located the maximum value of LSF, are found and stored as a shape distribution.

Optics EXPRESS

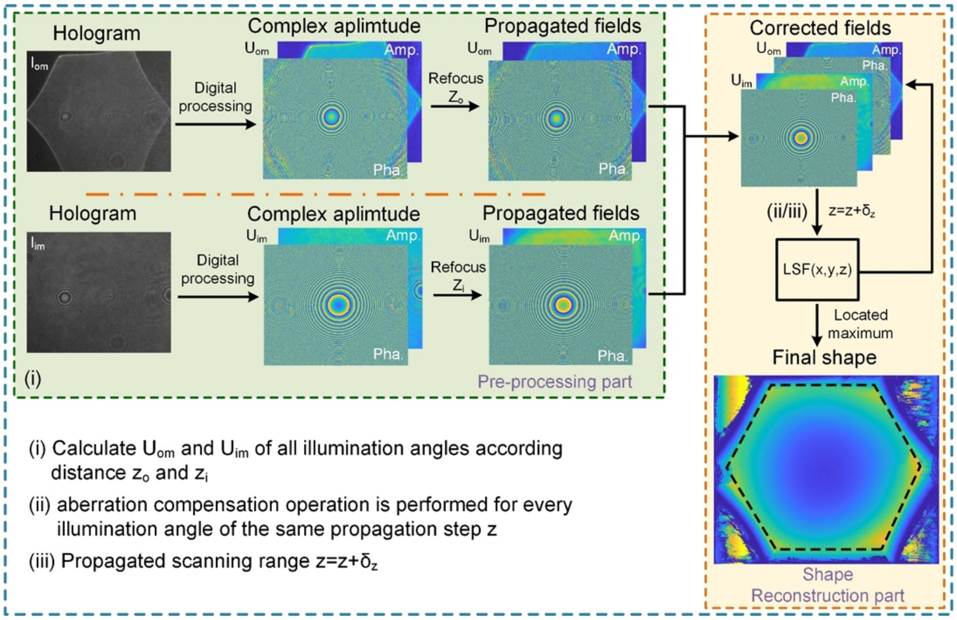

Fig. 5. Processing of shape-reconstruction algorithm with volumetric aberration compensation in spherical-wave illumination scanning.

Furthermore, it is worth mentioning that in this implementation, the summation part of the algorithm is only evaluated for the central area of the object wave spectrum. In order not to lose the sampling rate, after summation and before inverse FT, zero padding in the Fourier domain is applied. This improves the numerical efficiency of the algorithm.

To prove the viability of the reconstructed algorithm, we show the simulated reconstruction of the plane and spherical wave illumination scanning. For simplicity, we perform simulations using 1D information without considering the noise. We select the angular range [-30°, 30°], and the number of used angles is 61 with the step is 1°. The scanning range z is [-0.8 µm, 9 µm], and δz 0.0025 µm. The final retrieved results of the plane and spherical wave illumination scanning are shown in Fig. 6(a) and 6(b), respectively. It shows that these two illumination scanning methods have the ability to retrieve the shape profile of the simulated object.

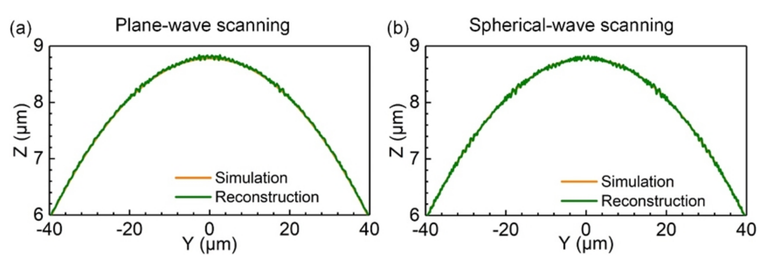

Fig. 6. The simulation results. (a) and (b) are the results of plane-wave and SWS, respectively.

The accuracy of the conventional holographic aberration compensation based on aberration subtraction for a case of large aperture field and deep measurements is investigated with simulation. The parameters of the scanning beam are taken from the experimental measurement of sample 3, where $z_s = 200$ µm. For simplicity, two plane-mirror objects with different depths are investigated.

Optics EXPRESS

One is at $z_d = 2$ µm from the focus, while for the second $z_d = 20$ µm. The assumed aberration is shown in Fig. 7(a). The simulations are realized in the steps: (1) the aberration is added to the illumination beam of z_s and scanning angle 0°, (2) the obtained beam is propagated by $2z_d$ to the focus plane, (3) the assumed aberration is subtracted at focus plane, (4) the result is propagated by z_d where aberration is compared with the aberrated object wave. The obtained retrieved results are shown in Fig. 7(b) and 7(c), and the cross-section profile along the x direction of the simulated aberration (orange line), aberration for 20 µm object (green line) and 2 µm object (blue line) is presented in Fig. 7(d). It is easy to find that the conventional aberration compensation has low accuracy for large aperture fields and deep measurements. However, the proposed method propagates the illumination and object waves separately, which will compensate for this disadvantage. The result, which is shown with a red line in Fig. 7(d), illustrates that the aberration of 20 µm depth object is almost compensated, guaranteeing the accuracy of reconstructed results. To better demonstrate the high performance of the proposed aberration compensation method, we calculate the structural similarity index (SSIM) for the results illustrated in Fig. 7. For the presented results, the proposed and conventional aberration compensation gives the SSIM values 1.00 and 0.03 for 20 µm object depth, respectively. For 2 µm depth, the conventional method provides SSIM = 0.44.

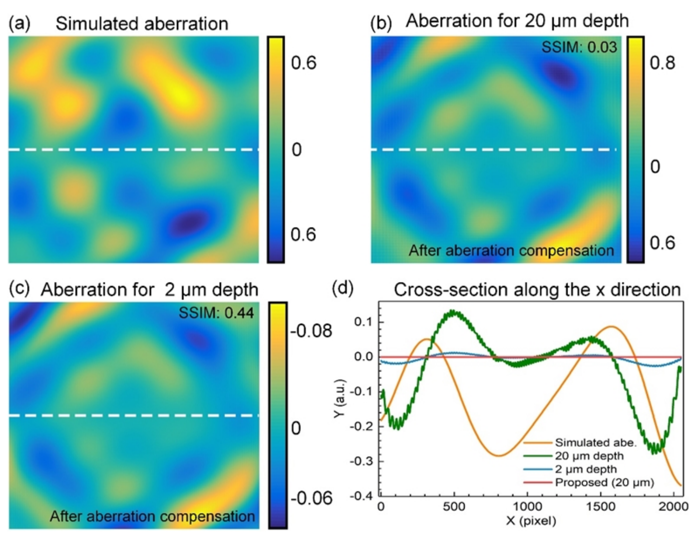

Fig. 7. Simulation results of using conventional aberration compensation method. (a) Simulated aberration. (b) and (c) are the conventional aberration compensation for 20 µm and 2 µm object depth, respectively. (d) The cross-sections along the x direction in the white dash line of (a-c).

3. Experimental results

This section presents the experimental verification of the proposed method and compares the reconstructed results two scanning approaches: spherical-wave and plane-wave. Firstly, the reconstructed surface and LSF results of a hexagonal object (sample 3) (measurement with a 50× microscope objective with 0.75 NA) prove that SWS can deliver undisturbed measurement data even for high-NA areas of the sample. Secondly, the results of sample 1 (a square object with lower $h_{\max}$ than sample 3) show that SWS offers slightly improved reconstruction compared to plane-wave illumination. Finally, we image sample 2 with a 20× microscope objective with 0.42 NA to show that SWS can successfully measure high-NA objects also using a lower

NA lens. Before illustrating the experiment, it is necessary to optimize the measurement with SWS illumination: (i) determining the z_s, which is the 2F optimization parameter, (ii) performing measurement of holograms using spherical-wave scanning, (iii) inspection of the result and if needed re-optimizing z_s and performing measurement with the corrected z_s, (iv) shape reconstruction using the reconstruction algorithm, as explained in Sec. 2.3. And we use Matlab 2020a and a computer with 3.3 GHz and 128 G RAM for reconstruction.

The first experiment compares the measurement capabilities of plane-wave scanning and SWS for a high-NA object (sample 3, as shown in Table 1). A series of fringe patterns were loaded into SLM to realize multi-angle plane-wave illumination scanning, as shown in Fig. 1(a_1). Meanwhile, SWS can be achieved by loading patterns generated using the focal length (z_s) 200 µm as the parameter of beam sphericity, as shown in Fig. 1(a_2). The selection of this sphericity is shown in Sec. 2.2. We selected a 50× microscope objective with 0.75 NA for measurement, and the angular range is [-30°, 30°], and 61 holograms were captured, which can guarantee the reconstructed accuracy but scarify the imaging speed. Then we used the reconstruction algorithm mentioned in Sec. 2.3 and set the scanning range z from −5 µm to 35 µm and δz is 0.1 µm. For this experiment and used parameters, the processing times of reconstruction algorithms for plane-wave and spherical-wave scanning are 270.4s and 426.1s, respectively. The final reconstructed results of plane and spherical wave illumination scanning for the same angular range are shown in Fig. 8(a) and 8(b). It was found that the SWS method can retrieve full information about a high-NA sample, and the cross-section profile of the SWS results along the x and y directions are continuous up to the edges of the hexagonal sample, are shown in Fig. 8(f) and 8(i). Plane-wave scanning method cannot achieve this, and on the reconstruction, we may observe the shape discontinuities and errors. DHP results are based on LSF parameters calculated from all scans. The shape of the LSF can indicate whether the illumination method used is able to adequately recover the shape of the test samples within the investigated measurement range. And the resulting LSF's along the x and y direction of these two different illumination scanning methods are shown in Fig. 8(d, e, g, h), respectively. It can be easily observed that the LSF of spherical-wave illumination scanning has a complete distribution in the measurement range, and thus the shape can be recovered.

Additionally, we prove how sample 3 is challenging for optical measurements. A white light interferometer (WLI) using a 51.8× magnification was used to measure the same sample. The result in Fig. 8(c) shows that the low-coherence optical profilometry method can measure only the central part of this object. Meanwhile, we compared the reconstructed results of using the conventional (the left of Fig. 9) and proposed (in Fig. 8(b)) aberration compensation methods. The enlarged areas of the same locations (① and ②) proved that the proposed method has a good ability to maintain high-accuracy surface profile results. Finally, all these results indicate that the SWS method is an appropriate scanning solution for high-NA samples.

Based on the above experiment, it can be seen that for sample 3, it was impossible to obtain information from the entire surface using plane-wave scanning and WLI. Therefore, a measurement of sample 1 (the information is shown in Table 1), with a lower NA than sample 3, is presented next. Here, the plane-wave scanning method is able to provide valuable measurement data. In this case, the same MO and scanning angular range are used to perform the experiment. The applied $z_s = 187$ µm was found using 2F optimization. Results obtained using plane-wave illumination scanning and SWS are shown in Fig. 10(a-c) and 10(e-g), respectively. Comparison of the holograms with an illumination angle of -28° of the plane-wave illumination scanning (Fig. 10(a)) and SWS (Fig. 10(e)) shows that for the plane-wave case, some information is lost (shadow in the bottom part of the hologram). The same is true for the 28° angle, as shown in Fig. 10(b) and 10(f). Comparing the reconstructions (as shown in Fig. 10(c) and 10(g)) and cross-sectioning profiles along the x and y direction (as shown in Fig. 10(d) and 10(h)) of the plane-wave illumination scanning and SWS, both illumination methods can retrieve this object well. However, SWS illumination reconstructed the border, giving better results than plane-wave

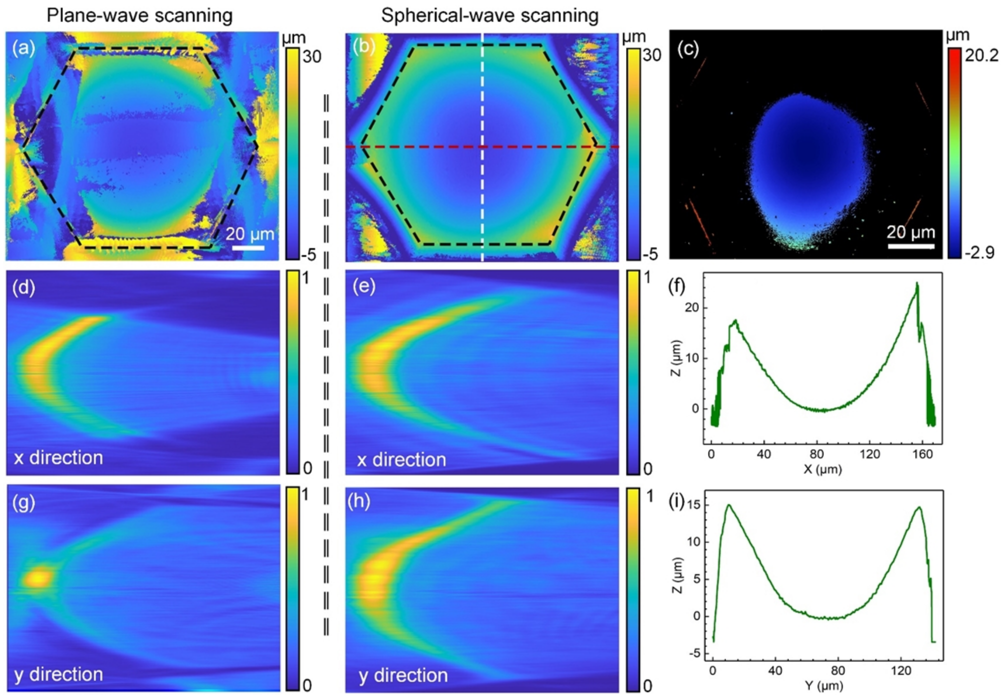

Fig. 8. Reconstructed results on imaging hexagon object (Sample 3). (a) and (b) are the surface results of plane-wave scanning and spherical-wave scanning, respectively. (c) Result of white light interferometry. (d, e, g, h) The LSF of two wave scanning illumination methods along the x and y directions. (f, i) The cross-sectioning profile along the x (red-dash) and y (white-dash) direction of (b).

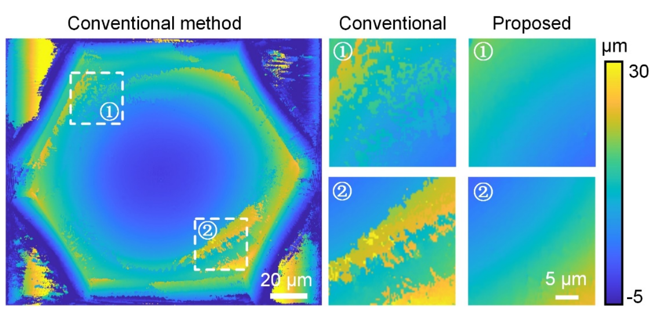

Fig. 9. Reconstructed results of using conventional and proposed aberration compensation methods. Two regions (① and ②) are enlarged to compare the difference between these methods.

illumination. This can be seen directly not only in Fig. 10(c) and 10(g) but also in the profiles (Fig. 10(d) and 10(h)) near the start and end of the cross-sectioning.

The final experimental results show technique merit when using lower NA optics in the SWS-DHP system, that in plane-wave illumination scanning DHP is still challenging. This merit can be verified using a 20× microscope objective with 0.42 NA to image sample 2 (the details are shown in Table 1) in the experiment. For SWS illumination, the parameter $z_s = 270\,\mu m$ was found by using the 2F method. The angular range is limited to [-17°, 17°] because of the limited NA of the microscope objective. As a result, 35 holograms were captured with an angular step of 1°.

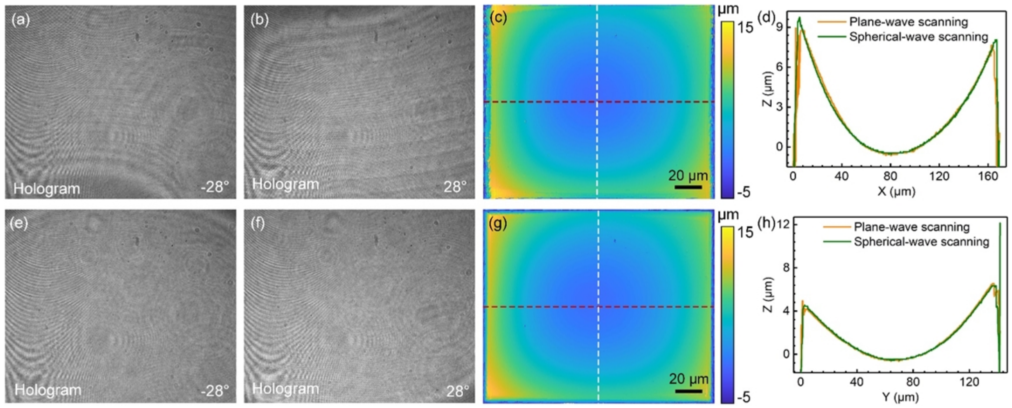

Fig. 10. Holograms and results of two wave scanning illumination methods on imaging square. (a-b) and (e-f) are the holograms of different illumination angles of plane-wave scanning and spherical-wave scanning, respectively. (c) and (g) are the reconstructed results. (d) and (h) are the cross-sectioning profile along the x (red-dash) and y (white-dash) direction in (c) and (g).

The holograms of three illumination angles (-17°, 0°, 17°) are shown in Fig. 11(a-c). An object area is marked by the orange-dash line in Fig. 11(b). After using the same algorithm shown in Sec. 2.3, the final results of shape reconstruction are shown in Fig. 11(d-f). These results prove our statement that SWS improves the digital holography profilometry technique and offers the possibility of measuring the high-NA samples even at lower NA optics.

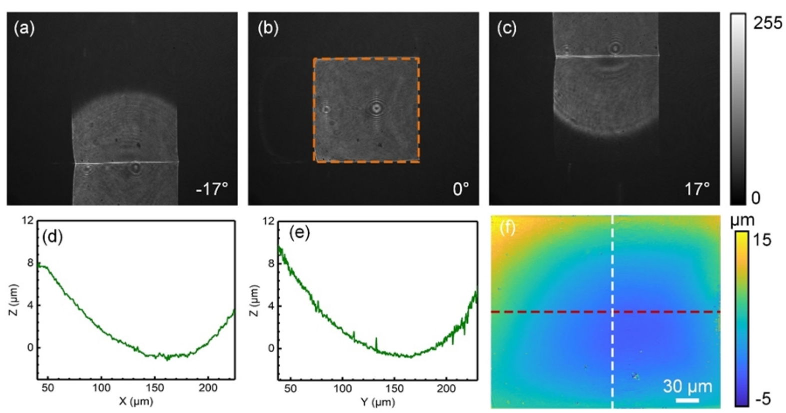

Fig. 11. Holograms and results of spherical-wave scanning illumination methods using 20×/0.42 NA microscope objective. (a-c) and (e-f) are the holograms of different illumination angles. (d) and (e) are the cross-sectioning profile along the x (red-dash) and y (white-dash) direction in the reconstructed result (f).

4. Conclusions

This study presents a novel measurement method named spherical-wave illumination scanning digital holographic profilometry (SWS-DHP), which can accurately measure the surface profile of the high-NA sample. For this, we introduce a 2F optimization method based on measuring the focal length of the object to determine the spherical scanning component. Depending on the NA of the measured object, the parameters of the spherical scanning beam need to be reoptimized to increase the information content of the holographic input data. Compared with the mechanically adjusted lens to introduce spherical-wave illumination, our method has higher precision and repeatability and is easier to control since it needs to load a series of generated patterns with different sphericity into SLM. To illustrate the merit of the SWS illumination method, comparison results on PS analysis of imaging high-NA samples with plane-wave illumination scanning and SWS are presented. Meanwhile, the traditional holographic aberration compensation method based on aberration subtraction has proven ineffective due to low accuracy for the large aperture holograms used in this work. Hence, a new shape reconstruction algorithm with volumetric and accurate aberration compensation based on the propagation of the measured object and illumination waves was proposed to obtain high-quality measurements. However, as mentioned above, the measurement range of the object is limited by the spherical component of SWS, meanwhile, the experiment requires capturing several holograms to maintain a high-accuracy shape reconstruction, which is time-consuming and unfavorable for dynamic process measurement. Hence, it is worth researching the improvement of imaging speed and keeping the same accuracy by reducing the illumination angles and steps or achieving a single-shot multi-angle illumination by combining the spherical-wave illumination and finding the optimized parameters of SWS to ensure the measurement range will be the direction of improvement in future work.

Funding. Narodowe Centrum Nauki (UMO-2018/31/B/ST7/02980); Politechnika Warszawska; China Scholarship Council; Ministry of Science and ICT, South Korea (IITP, No. 2020-0-00981).

Acknowledgments. T. Kozacki and H-C. Choo supervised the project. K. Wen, M.S. Idicula, and M. Józwik performed experiments and data analysis. K. Wen, M.S. Idicula, P. Gao and T. Kozacki wrote the draft of the manuscript; All the authors edited the manuscript.

Disclosures. The authors declare that there are no conflicts of interest related to this article.

Data availability. Data underlying the results presented in this paper are not publicly available at this time but may be obtained from the authors upon reasonable request.

References

1. P. Gao and C. Yuan, "Resolution enhancement of digital holographic microscopy via synthetic aperture: a review," Light: Adv. Manuf. **3**(1), 105–120 (2022).
2. B. Javidi, A. Carnicer, A. Anand, *et al.*, "Roadmap on digital holography," Opt. Express **29**(22), 35078–35118 (2021).
3. V. Micó, J. Zheng, J. Garcia, *et al.*, "Resolution enhancement in quantitative phase microscopy," Adv. Opt. Photonics **11**(1), 135–214 (2019).
4. T. Zeng, Y. Zhu, and E. Y. Lam, "Deep learning for digital holography: a review," Opt. Express **29**(24), 40572–40593 (2021).
5. T. Nguyen, V. Bui, V. Lam, *et al.*, "Automatic phase aberration compensation for digital holographic microscopy based on deep learning background detection," Opt. Express **25**(13), 15043–15057 (2017).
6. S. Ma, R. Fang, Y. Luo, *et al.*, "Phase-aberration compensation via deep learning in digital holographic microscopy," Meas. Sci. Technol. **32**(10), 105203 (2021).
7. M. S. Idicula, T. Kozacki, M. Józwik, *et al.*, "Multi-Incidence Holographic Profilometry for Large Gradient Surfaces with Sub-Micron Focusing Accuracy," Sensors **22**(1), 214 (2021).
8. J. Martinez-Carranza, M. Mikuła-Zdańkowska, M. Ziemczonok, *et al.*, "Multi-incidence digital holographic profilometry with high axial resolution and enlarged measurement range," Opt. Express **28**(6), 8185–8199 (2020).
9. T. Kozacki, M. Mikuła-Zdańkowska, J. Martinez-Carranza, *et al.*, "Single-shot digital multiplexed holography for the measurement of deep shapes," Opt. Express **29**(14), 21965–21977 (2021).
10. D. J. Lee and A. M. Weiner, "Optical phase imaging using a synthetic aperture phase retrieval technique," Opt. Express **22**(8), 9380–9394 (2014).
11. P. Gao, G. Pedrini, and W. Osten, "Structured illumination for resolution enhancement and autofocusing in digital holographic microscopy," Opt. Lett. **38**(8), 1328–1330 (2013).
12. K. Wen, Z. Gao, R. Liu, *et al.*, "Structured illumination phase and fluorescence microscopy for bioimaging," Appl. Opt. **62**(18), 4871–4879 (2023).
13. K. Liżewski, T. Kozacki, and J. Kostencka, "Digital holographic microscope for measurement of high gradient deep topography object based on superresolution concept," Opt. Lett. **38**(11), 1878–1880 (2013).
14. T. Kozacki, K. Liżewski, and J. Kostencka, "Absolute shape measurement of high NA focusing microobjects in digital holographic microscope with arbitrary spherical wave illumination," Opt. Express **22**(14), 16991–17005 (2014).
15. J. Dong, C. Jiang, and S. Jia, "Digital holographic metrology based on multi-angle interferometry," Opt. Lett. **41**(18), 4301–4304 (2016).

Optics EXPRESS

16. M. Mikuła, T. Kozacki, M. Józwik, *et al.*, "Accurate shape measurement of focusing microstructures in Fourier digital holographic microscopy," Appl. Opt. **57**(1), A197–A204 (2018).
17. M. Józwik, M. Mikuła, T. Kozacki, *et al.*, "Topography measurements of high NA aspherical microlenses by digital holographic microscopy with spherical illumination," Proc. SPIE **10329**, 103290C (2017).
18. K. Liżewski, S. Tomczewski, T. Kozacki, *et al.*, "High-precision topography measurement through accurate in-focus plane detection with hybrid digital holographic microscope and white light interferometer module," Appl. Opt. **53**(11), 2446–2454 (2014).
19. C. Wagner, W. Osten, and S. Seebacher, "Direct shape measurement by digital wavefront reconstruction and multi-wavelength contouring," Opt. Eng. **39**(1), 79–85 (2000).
20. A. Wada, M. Kato, and Y. Ishii, "Large step-height measurements using multiple-wavelength holographic interferometry with tunable laser diodes," J. Opt. Soc. Am. A **25**(12), 3013–3020 (2008).
21. C. C. Aleksoff, "Multi-wavelength digital holographic metrology," Proc. SPIE **6311**, 63111D (2006).
22. C. J. Mann, P. R. Bingham, V. C. Paquit, *et al.*, "Quantitative phase imaging by three-wavelength digital holography," Opt. Express **16**(13), 9753–9764 (2008).
23. P. Gao, B. Yao, R. Rupp, *et al.*, "Autofocusing based on wavelength dependence of diffraction in two-wavelength digital holographic microscopy," Opt. Lett. **37**(7), 1172–1174 (2012).
24. M. K. Kim, "Phase microscopy and surface profilometry by digital holography," Light Adv. Manuf. **3**, 481–492 (2022).
25. J. Pomarico, R. Arizaga, H. Rabal, *et al.*, "Digital holographic contouring," Opt. Commun. **98**(4-6), 257–260 (1993).
26. I. Yamaguchi, S. Ohta, and J.-i. Kato, "Surface contouring by phase-shifting digital holography," Opt. Lasers Eng. **36**(5), 417–428 (2001).
27. V. Srivastava, S. Nandy, and D. Singh Mehta, "High-resolution full-field spatial coherence gated optical tomography using monochromatic light source," Appl. Phys. Lett. **103**(10), 103702 (2013).
28. N. Ph, R. Völkel, H. P. Herzig, *et al.*, "Design, fabrication and testing of microlens arrays for sensors and microsystems," Pure Appl. Opt. **6**(6), 617–636 (1997).
29. M. Testorf, B. Hennelly, and J. Ojeda-Castañeda, *Phase-space optics: fundamentals and applications* (McGraw-Hill Education, 2010).
30. J. W. Goodman, *Introduction to Fourier optics* (Roberts and Company publishers, 2005).
31. T. Kozacki and J. Winnik, "Scattering of arbitrary wave from 3D dielectric surfaces by Born series expansion," OSA Technical Digest, W3A.8 (2019).
32. M. Born and E. Wolf, *Principles of optics: electromagnetic theory of propagation, interference and diffraction of light* (Cambridge University Press, New York, 1999).
33. A. Rohrbach and W. Singer, "Scattering of a scalar field at dielectric surfaces by Born series expansion," J. Opt. Soc. Am. A **15**(10), 2651–2659 (1998).
34. T. Kozacki, K. Falaggis, and M. Kujawinska, "Computation of diffracted fields for the case of high numerical aperture using the angular spectrum method," Appl. Opt. **51**(29), 7080–7088 (2012).